

# Sympathetic Ground State Cooling and Time-dilation Shifts in an $^{27}\text{Al}^+$ Optical Clock

J.-S. Chen,<sup>1,2</sup> S. M. Brewer,<sup>1</sup> D. B. Hume,<sup>1</sup> C. W. Chou,<sup>1</sup> D. J. Wineland,<sup>1,2</sup> and D. R. Leibbrandt<sup>1,2,\*</sup>

<sup>1</sup>*Time and Frequency Division, National Institute of Standards and Technology, Boulder, Colorado, 80305, USA*

<sup>2</sup>*Department of Physics, University of Colorado, Boulder, Colorado, 80309, USA*

(Dated: March 9, 2022)

We report Raman sideband cooling of  $^{25}\text{Mg}^+$  to sympathetically cool the secular modes of motion in a  $^{25}\text{Mg}^+ - ^{27}\text{Al}^+$  two-ion pair to near the three-dimensional (3D) ground state. The evolution of the Fock state distribution during the cooling process is studied using a rate-equation simulation, and various heating sources that limit the efficiency of 3D sideband cooling in our system are discussed. We characterize the residual energy and heating rates of all the secular modes of motion and estimate a secular motion time-dilation shift of  $-(1.92 \pm 0.11) \times 10^{-18}$  for an  $^{27}\text{Al}^+$  clock at a typical clock probe duration of 150 ms.

PACS numbers: 37.10.Rs, 37.10.Ty

Trapped and laser-cooled ions are useful for many applications in quantum information and quantum metrology because of their good isolation from the ambient environment and strong mutual Coulomb interaction between ions [1–6]. The Coulomb interaction establishes shared normal modes of motion, called secular modes, which enable information exchange and entanglement between ions. For many operations in quantum information and metrology, these secular modes should ideally be prepared in their ground state. In state-of-the-art trapped-ion optical clocks [7], uncertainty in the Doppler shift due to the residual excitation of these modes is a dominant contribution to the total clock uncertainty [8–10].

All trapped-ion optical clocks to date have been operated with the ions' motion near the Doppler cooling limit [8, 10]. For clocks based on quantum-logic spectroscopy of the  $^1S_0 \leftrightarrow ^3P_0$  transition in  $^{27}\text{Al}^+$ , the smallest uncertainty has been achieved by performing continuous sympathetic Doppler cooling on the logic ion ( $^{25}\text{Mg}^+$ ) during the clock interrogation [8]. Due to the difficulty of performing accurate temperature measurements of trapped ions near the Doppler cooling limit, the uncertainty of the secular motion temperature was limited to 30% in this clock.

To reduce both the secular motion time-dilation shift and its uncertainty, an obvious approach is to use sub-Doppler cooling techniques [11–15]. However, these schemes have not previously been implemented due to high ambient motional heating rates, the need for extra cooling laser beams, and the difficulty of characterizing the resulting motional state distribution which can be non-thermal [8, 10, 16]. For sideband cooling, a non-thermal distribution can result from zero-crossings in the cooling Rabi frequency as a function of the Fock state [17, 18] and from using cooling durations insufficient to reach equilibrium. Although sideband cooling can reach extremely low energy, a very small non-thermal component can have an important effect. This makes the estimation of the time-dilation shift quite challenging.

Here we demonstrate sympathetic cooling of a

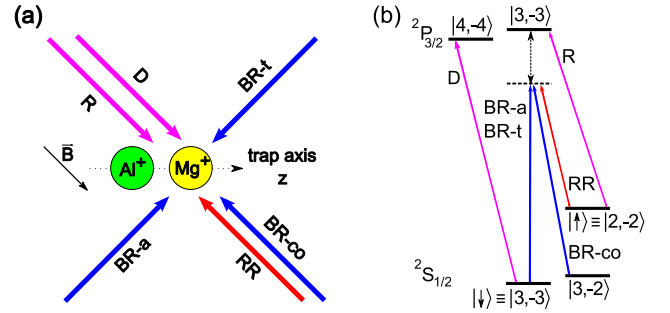


FIG. 1: (color online). (a)  $^{25}\text{Mg}^+$  laser beam geometry. (b)  $^{25}\text{Mg}^+$  energy level diagram (not-to-scale). Quantum states  $|F, m_F\rangle$  are labeled by the total angular momentum  $F$  and the projection along the quantization direction  $m_F$ . Raman laser detuning from the transition  $|\downarrow(\uparrow)\rangle \leftrightarrow |^2P_{3/2}, F=3, m_F=-3\rangle$  is approximately 50 GHz and the magnetic field is about 1 Gauss. D: Doppler cooling. R: repumping. RR: red Raman. BR-a: axial blue Raman. BR-t: transverse blue Raman. BR-co: co-propagating blue Raman.

$^{25}\text{Mg}^+ - ^{27}\text{Al}^+$  two-ion pair to the 3D motional ground state with high probability. This is accomplished with Raman sideband cooling in an ion trap with motional heating rates two orders of magnitude lower than those achieved in previous  $^{27}\text{Al}^+$  clocks. The evolution of the Fock state distribution during the cooling process is investigated by using a rate-equation simulation which is verified by comparison with experimental measurements. The cooling pulse sequence is optimized according to the model. We discuss the various heating mechanisms as well as the secular motion time-dilation uncertainty in this system.

One  $^{25}\text{Mg}^+$  and one  $^{27}\text{Al}^+$  are trapped simultaneously in a linear Paul trap to form a pair aligned along the trap axis. The energy levels of  $^{25}\text{Mg}^+$  and the laser beam geometry are shown in Fig. 1. We define the z-axis to be along the trap axis while x and y represent two directions orthogonal to z. Along each axis there

are two motional modes, the COM mode where the motional vectors of two ions are in the common direction and the “stretch” (STR) mode where they are opposite. Our trap is operated with axial mode frequencies in the range of 2.7 to 5 MHz and transverse mode frequencies in the range of 5 to 7.5 MHz [19]. We begin each experiment with 2 ms of Doppler cooling on the  $^{25}\text{Mg}^+ |\downarrow\rangle \equiv |^2S_{1/2}, F=3, m_F=-3\rangle \leftrightarrow |^2P_{3/2}, F=4, m_F=-4\rangle$  cycling transition to cool all six motional modes close to the Doppler limit and prepare  $^{25}\text{Mg}^+$  in  $|\downarrow\rangle$ . The subsequent sideband cooling and motional state diagnosis are implemented with stimulated Raman transitions between the  $|\downarrow\rangle$  and  $|\uparrow\rangle \equiv |^2S_{1/2}, F=2, m_F=-2\rangle$  states. To cool the secular motion in three orthogonal directions efficiently, we have two sets of Raman beams as shown in Fig. 1 (a). The axial (BR-a) and transverse (BR-t) blue Raman beams in combination with the red Raman beam (RR) generate the differential wavevectors to cool the axial and transverse modes of motion respectively. All Raman laser beams are transmitted through optical fibers for mode filtering and reduction of beam-pointing fluctuations [20]. Throughout the paper, “carrier” pulses denote transitions with no change in motional quanta, while red-sideband (RSB) and blue-sideband (BSB) pulses correspond to  $|\downarrow, n\rangle \rightarrow |\uparrow, n-\Delta n\rangle$  and  $|\downarrow, n\rangle \rightarrow |\uparrow, n+\Delta n\rangle$  transitions respectively, where  $n$  is the initial Fock state and  $\Delta n$ , the order of the sideband transition, represents the number of quanta changed in a single pulse. After a RSB cooling transition,  $^{25}\text{Mg}^+$  is in  $|\uparrow\rangle$  which is then optically pumped to  $|\downarrow\rangle$  by applying a repumping pulse sequence. Each repumping pulse drives the  $|\uparrow\rangle$  to  $|^2P_{3/2}, F=3, m_F=-3\rangle$  transition, followed by a carrier transition between  $|\uparrow\rangle$  and  $|^2S_{1/2}, F=3, m_F=-2\rangle$  by applying RR and BR-co simultaneously. The  $^{25}\text{Mg}^+$  atomic state is determined at the end of each experiment by collecting photons scattered from the cycling transition and converting the photon count histogram to the transition probability using a maximum-likelihood estimation [19].

In general, when the amplitude of the ion motion is not negligible compared with the effective Raman transition wavelength, the resolved sideband cooling becomes complicated due to the presence of Fock-state population “traps” where the Rabi rate of the RSB transition approaches zero [17, 18]. For example, the z-COM mode with Lamb-Dicke parameter  $\eta = 0.18$  (frequency = 2.7 MHz) has a zero-crossing of the 1<sup>st</sup> order RSB Rabi rate near the Fock state  $n = 44$ . Numerical simulations indicate that the 2<sup>nd</sup> order RSB pulses are significantly more efficient at reducing populations in high Fock states, depending on the Lamb-Dicke parameter and the overhead time spent on operations like repumping during each cooling cycle. Multiple 2<sup>nd</sup> order RSB cooling pulses are applied before the 1<sup>st</sup> order RSB pulses for two axial modes in our experiment. After sideband cooling, all RSB signals vanish, which indicates that the two-ion pair

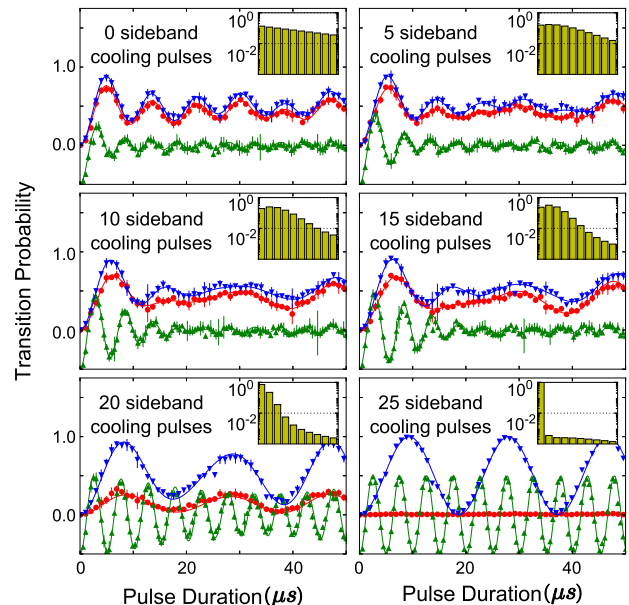


FIG. 2: (color online). Rabi oscillations of the 1<sup>st</sup> RSB (red, circle), the 1<sup>st</sup> BSB (blue, down triangle) and carrier (green, up triangle) Raman transitions of the axial mode for a single  $^{25}\text{Mg}^+$  after different numbers of pulses in the sideband cooling sequence. Carrier Rabi oscillation curves are shifted by  $-0.5$  for visibility. The cooling sequence consists of 17 2<sup>nd</sup> order RSB pulses followed by 8 1<sup>st</sup> order RSB pulses to prepare the ion near the motional ground state. Data points are the average of about 1000 experiments. Solid lines are given by the rate equation simulation without any free parameters [19]. The simulated population evolution of the first 10 Fock states during the cooling process are shown in insets. We include 150 of Fock states in the simulation.

is close to the 3D motional ground state [19].

A sensitive method to determine the residual motional excitation is to measure the ratio of the BSB and RSB transition probabilities [11, 12]. However, this method is accurate only in the case of thermal equilibrium, which is generally not true for populations after sideband cooling [21]. To overcome this problem, we have developed a rate equation model to simulate the sideband cooling process. We model the cooling dynamics using the coherent RSB transition probability [22]

$$P_{\uparrow, n_p}(t) = \frac{1}{2} (1 - e^{-\gamma t} \cos(2\Omega_{n_p, n_p + \Delta n_p} t)) P_{\downarrow, n_p + \Delta n_p}(0), \quad (1)$$

where  $\Delta n_p$  is the order of the RSB pulse,  $\Omega_{n_p, n_p + \Delta n_p}^{(p)}$  is the sideband Rabi rate for the transition  $|\downarrow, n_p + \Delta n_p\rangle \rightarrow |\uparrow, n_p\rangle$ ,  $\gamma$  is the decoherence rate, and  $t$  is the duration of the RSB pulse. Following Ref. [23], we have also included heating mechanisms that treat the heating as an interaction with a thermal reservoir. We validate our model by comparing it with experimental data at intermediate times during the cooling sequence. Separate calibrations for the Rabi

rates, decoherence rates, and Lamb-Dicke parameters, in combination with the Fock state distributions from our simulation, are used to produce Rabi-oscillation curves of the secular motion along the z direction for a single  $^{25}\text{Mg}^+$  with no free parameters. As shown in Fig. 2, Rabi oscillations from our simulation yield good agreement with experimental data throughout the sideband cooling process. Simulation results also reveal the non-thermal distribution after sideband cooling [19]. Our simulation indicates the energy of ions after sideband cooling may be underestimated by orders of magnitude in certain situations if it is measured using the BSB-RSB ratio method under the assumption of thermal equilibrium.

During the sideband cooling process, ions experience recoil from both Raman cooling beams and repumping pulses. The recoil heating due to Raman beams arises from transitions through the  $|^2P_{3/2}\rangle$  excited states. The heating rate due to Raman scattering is estimated to be  $< 10^{-4} \mu\text{s}^{-1}$  both theoretically and via calibration experiments on a single  $^{25}\text{Mg}^+$  for a given Raman beam intensity [24]. The Rayleigh scattering rate due to the Raman beams is estimated to be about 50% of the Raman scattering rate in our experiment [25]. The heating from Raman beams does not depend on the frequency difference between the two Raman beams and all motional modes will heat each time the Raman beams are applied to the ions. For this reason, while the heating rates are small this mechanism contributes significantly to the ions' final energy.

The recoil heating in the repumping sequence is measured directly by preparing ions in the motional ground state and then repeating a carrier pulse followed by a repumping sequence multiple times to extract the heating rate per repumping cycle. This heating scales with  $\eta^2$  and is about 0.027 quanta per repumping cycle per spin excitation in z-COM mode. Although this value is relatively large, the effective heating due to repumping needs to be multiplied by the amount of population not in the ground state, and becomes negligible at the end of the sideband cooling process.

Effects of off-resonant coupling to the carrier transition during RSB pulses are discussed in [12]. For an ion in the motional ground state, the probability of motional excitation due to this mechanism scales as  $1/\omega_\nu^2$ , where  $\omega_\nu$  is the motional frequency. Another important source of heating results from the combination of spontaneous emission due to Raman beams and the RSB pulses. After a spontaneous decay to  $|\uparrow\rangle$ , the RSB pulse will add one motional quantum to the mode addressed. The probability of motional excitation due to this mechanism depends on the RSB pulse duration and scales as  $1/\eta$ . Heating from electric field noise is measured as  $\dot{\bar{n}} \approx 10 \text{ s}^{-1}$  and  $1 \text{ s}^{-1}$  for the COM and STR modes, respectively [19]. The heating due to off-resonant coupling to the BSB transitions is not considered in our simulation because of the relatively small transition rate which scales as  $\eta^2/\omega_\nu^2$ .

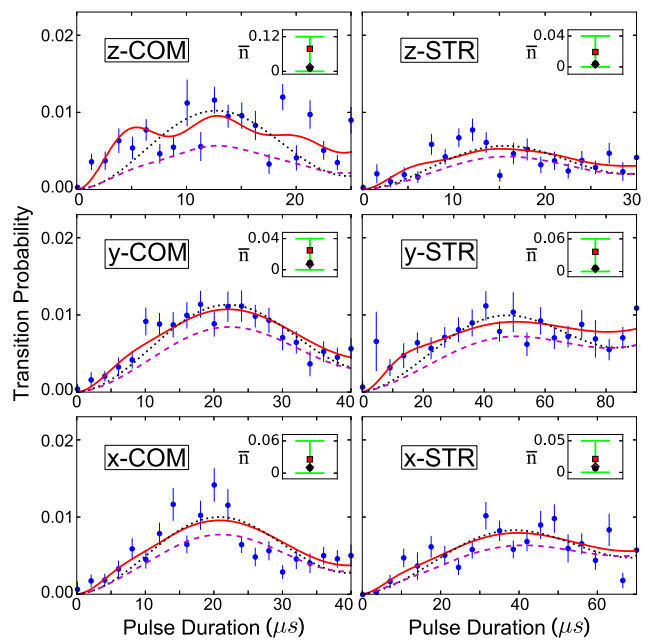


FIG. 3: (color online). Red sideband Rabi oscillations of the six  $^{25}\text{Mg}^+ - ^{27}\text{Al}^+$  motional modes after Raman sideband cooling. Blue data points are the average of about 50 000 experiments and the error bars are the standard deviation of the mean. Solid line: double-thermal distribution fit. Dotted line: single-thermal distribution fit. Dashed line: rate-equation simulation. The inset in each plot represents the average occupation number from fits and the simulation. Diamond: rate-equation simulation. Circle: single thermal distribution fit. Square: double thermal distribution fit. Circles overlay diamonds to within less than the size of the symbol. Green error bars represent the experimental uncertainties of average occupation numbers after sideband cooling. Upper bound of energy is given by the 95% confidence interval of the double thermal distribution fit.

To experimentally constrain the motional energy after Raman sideband cooling, we focus on Rabi oscillations of RSB transitions to investigate the population not in the ground state. Motivated by the simulation results, we fit our experimental data to a linear combination of two thermal distributions [19]. Simulation results, fits, and experimental data are plotted together in Fig. 3. The mean occupation number,  $\bar{n}$ , extracted from different methods and the energy uncertainties after sideband cooling are shown in the inset of each plot. The upper bound of this uncertainty is given by the 95% confidence interval of the fit to the double thermal distribution, which tends to give the highest energy compared to our simulation and the estimate from single thermal distribution fit, and the lower bound is set to zero.

To further verify that all motional modes of the  $^{25}\text{Mg}^+ - ^{27}\text{Al}^+$  two-ion pair are cooled close to the zero-point energy, we compare the Rabi oscillation frequencies of the  $^{27}\text{Al}^+ \ ^1S_0 \leftrightarrow \ ^3P_0$  carrier clock transition in

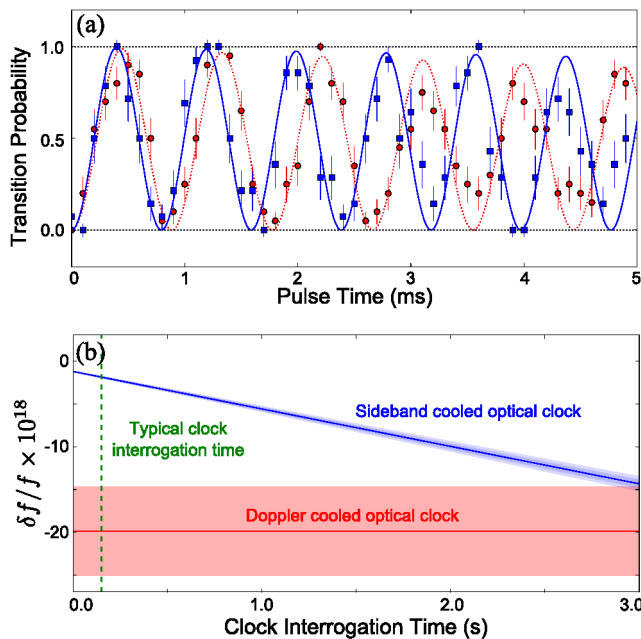


FIG. 4: (color online). (a) Rabi oscillation of  $^{27}\text{Al}^+ 1S_0 \leftrightarrow 3P_0$  carrier clock transition. Red circles: continuous sympathetic Doppler cooling,  $\Omega_{\text{Doppler}} = 2\pi \times 1.126(3)$  kHz. Blue squares: 3D sideband cooling,  $\Omega_{sc} = 2\pi \times 1.258(6)$  kHz. Lines are from fitting to an exponential decaying sinusoidal function. (b) Comparison of the time dilation shift due to the secular motion in two different clock operating conditions. Blue: clock operating near the motional ground state. Solid line is the fractional frequency shift and the region in blue represents the uncertainty. For a typical clock interrogation time of 150 ms, the secular motion time-dilation shift is  $-(1.92 \pm 0.11) \times 10^{-18}$ . Red: clock operating at the Doppler limit. A shift of  $-(19.9 \pm 5.2) \times 10^{-18}$  is reported in Ref. [8] including the secular motion time-dilation shift and the AC Stark shift from the Doppler cooling light.

two conditions and show results in Fig. 4(a). We first operate the clock near the Doppler limit by sympathetic Doppler cooling during the clock interrogation. Since the damping rate from the Doppler cooling is much larger than the Rabi rate of the clock transition, the entire Fock state distribution is averaged over a thermal distribution during a single clock pulse and the Rabi oscillation maintains coherence. In a second experiment we operate the clock by sideband-cooling all motional modes before the clock interrogation pulse. We expect the Rabi rate of the Doppler cooled optical clock ( $\Omega_{\text{Doppler}}$ ) will be 11(2)% smaller than that of the sideband cooled optical clock ( $\Omega_{sc}$ ) due to the Debye-Waller effect [22],

$$\frac{\Omega_{\text{Doppler}}}{\Omega_{sc}} = \prod_p e^{-\eta_p^2 \bar{n}_p}, \quad (2)$$

where  $\eta_p$  and  $\bar{n}_p$  represent the Lamb-Dicke parameter of  $^{27}\text{Al}^+$  and the average occupation number at the Doppler

limit of motional mode  $p$  respectively. The uncertainty of the prediction is due to the uncertainty in the motional energy estimation near the Doppler limit. Experimentally, we observe a 10.5(4)% difference between the two clock operating conditions, which agrees with the theoretical prediction.

After preparing ions in the 3D motional ground state, there is no additional cooling light during the clock interrogation and we can eliminate the associated light shift reported in the previous  $^{27}\text{Al}^+$  optical clocks [8]. The average occupation number of the ions in a specific motional mode  $p$  during a clock interrogation of duration  $t_i$  can be expressed as

$$\langle n_p(t_i) \rangle = \bar{n}_{p,0} + \frac{1}{2} \dot{\bar{n}}_p t_i, \quad (3)$$

where  $\bar{n}_{p,0}$  is the energy after sideband cooling given in Fig. 3 and  $\dot{\bar{n}}_p$  is the heating rate due to the ambient electric field noise. Angle brackets denote an average over the clock interrogation time. A comparison of the secular motion time-dilation shift using sideband cooling here with continuous Doppler cooling from Ref. [8] is shown in Fig. 4(b). The heating rates of motional modes are the average of many measurements spanning several weeks [19]. Using the  $2\sigma$  uncertainty of our heating rate data to estimate the secular motion time-dilation shift uncertainty, we expect  $\delta f/f = -(1.92 \pm 0.11) \times 10^{-18}$  for 150 ms of clock interrogation time [19]. The overall frequency shift is dominated by the zero-point energy, which can be accurately determined, and the uncertainty is dominated by the energy uncertainty after sideband cooling. This is roughly an order of magnitude reduction in the shift and a factor of 50 reduction in the uncertainty due to secular motion time-dilation in comparison with  $-(16.3 \pm 5.0) \times 10^{-18}$  reported in the previous  $^{27}\text{Al}^+$  optical clock [8]. Extending the clock interrogation time to 1 s [26–29], the fractional time-dilation shift due to secular motion is estimated to be  $-(5.7 \pm 0.3) \times 10^{-18}$ .

In conclusion, we have sympathetically cooled a  $^{25}\text{Mg}^+ - ^{27}\text{Al}^+$  two-ion pair to the 3D motional ground state using stimulated Raman sideband cooling. A rate-equation simulation including various heating sources has been performed to characterize the secular motion energy of the ions in our ion trap. The results from the rate-equation simulation show agreement with experimental data throughout the sideband cooling process. The fractional frequency shift due to secular motion in the  $^{27}\text{Al}^+ 1S_0 \leftrightarrow 3P_0$  clock transition is estimated based on the characterization of ion motion and heating rate measurements. The shift due to secular motion time-dilation is reduced by an order of magnitude while the uncertainty is reduced by a factor of 50 in comparison with the previous  $^{27}\text{Al}^+$  optical clock. Our model may benefit other experiments utilizing sideband cooling to design efficient cooling pulse sequences that reduce experimental dead time. Our method is directly applicable

to other ion optical clocks for operation near the motional ground state to reduce the clock uncertainty.

We thank T. Rosenband for useful discussions. We thank Y. Lin and T. R. Tan for the careful reading of the manuscript. This work was supported by the Defense Advanced Research Projects Agency and the Office of Naval Research. S.M.B. was supported by the U.S. Army Research Office through a MURI grant W911NF-11-1-0400. This paper is a contribution of the U.S. government, and not subject to U.S. copyright.

## SUPPLEMENTAL MATERIAL

### Electronic State Detection

In our experiment, the mean photon counts collected during the detection time of  $250 \mu\text{s}$  from  $|\downarrow\rangle$  and  $|\uparrow\rangle$  are about 8 and 0.9, respectively, and the two counts histograms overlap significantly as shown in Fig. 5. The observed histograms in the experiment typically result from the scattered photons from a linear combination of two states and we find that applying a threshold to the photon counts is not sufficient to extract state populations at the 0.1% level. To extract the probability in  $|\downarrow\rangle$ , we use a maximum-likelihood estimation method to analyze our data. Before experiments start, we need two reference histograms,  $\mathcal{P}(k|\downarrow)$  and  $\mathcal{P}(k|\uparrow)$ , corresponding to the probability of observing  $k$  photons in  $|\downarrow\rangle$  and  $|\uparrow\rangle$ , respectively. We determine reference histograms experimentally by taking fluorescence measurements when the ions are prepared in the states of  $|\uparrow\rangle$  or  $|\downarrow\rangle$ . The state  $|\downarrow\rangle$  is prepared by applying a repumping pulse sequence after Doppler cooling while  $|\uparrow\rangle$  is prepared by applying a microwave  $\pi$  pulse from  $|\downarrow\rangle$ . During the experiment, we record a series of photon counts  $\{k_i\}$  from a particular quantum state  $|\Psi\rangle = \sqrt{p}|\downarrow\rangle + \sqrt{(1-p)}e^{i\phi}|\uparrow\rangle$  in  $m$  measurements, where  $p$  denotes the probability in  $|\downarrow\rangle$  and  $\phi$  is the relative phase between  $|\downarrow\rangle$  and  $|\uparrow\rangle$ . The errors in preparation of  $|\downarrow\rangle$ ,  $|\uparrow\rangle$  and the superposition states are negligible and do not contribute significantly to the determination of the kinetic energy. For a binomial system, the likelihood function is defined as,

$$\mathcal{L}(p) = \prod_{i=1}^m (p\mathcal{P}(k_i|\downarrow) + (1-p)\mathcal{P}(k_i|\uparrow)). \quad (4)$$

By maximizing the likelihood function numerically, we can estimate the probability in  $|\downarrow\rangle$  for any histogram observed in the experiments [30].

### Simulation and Ion Motional Energy Estimate

In the simulation, we treat a RSB pulse duration as a single time step and deal with the heating of the population in  $|\downarrow\rangle$  and  $|\uparrow\rangle$  after a RSB pulse as separate processes.

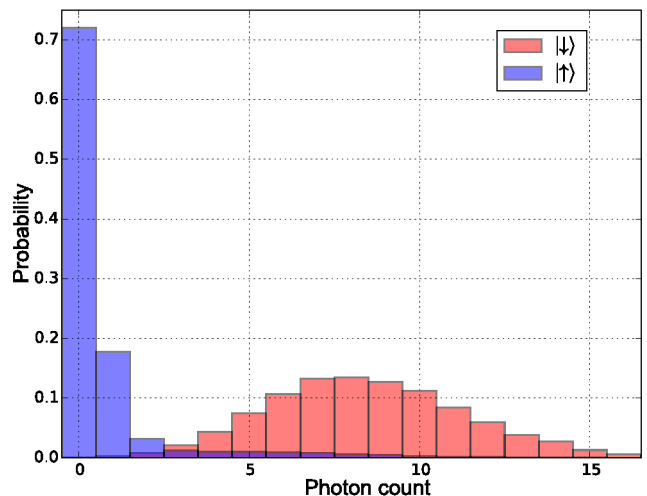


FIG. 5: Typical photon histograms scattered from  $|\downarrow\rangle$  and  $|\uparrow\rangle$ .

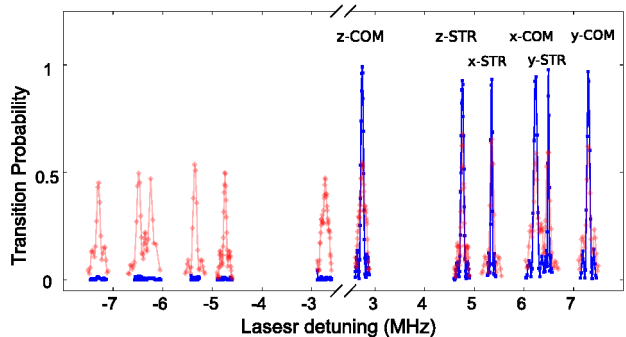


FIG. 6: Raman transition spectrum of a  $^{25}\text{Mg}^+ - ^{27}\text{Al}^+$  two-ion pair with all six secular modes of motion resolved. Red: after Doppler cooling. Blue: after Raman sideband cooling.

When a  $\Delta p_n$ -th order RSB cooling pulse of the duration  $t$  is applied to mode  $p$ , the population in  $|\uparrow\rangle$  is given by,

$$P_{\uparrow}(t) = \sum_{n_p=0}^{\infty} P_{\uparrow, n_p}(t), \quad (5)$$

where  $P_{\uparrow, n_p}$  is given by Eq. (1) in the main text. During the pulse, ions will heat primarily from the off-resonant carrier transition, and the combination of spontaneous decay and the RSB pulse, which are discussed in the main text. Since we are primarily interested in the final steady state, to include these two mechanisms in our model, we calculate the motional excitation rate from  $|\downarrow, n=0\rangle$  by solving the optical Bloch equation and only including quantum states  $|\downarrow, n=0\rangle$ ,  $|\downarrow, n=1\rangle$ , and  $|\uparrow, n=0\rangle$ . The heating values are summarized in Table II. This assumption will affect the sideband cooling time constant but not the achievable cooling limit because most of the population is in  $|\downarrow, n=0\rangle$  and  $|\downarrow, n=1\rangle$  at the end of

the cooling process. These two mechanisms mainly affect the mode  $p$  while the heating for the rest of the motional modes is through Raman and Rayleigh scattering during the pulse. In addition, all modes will experience recoil heating due to the repumping sequence. In general, we include 150 Fock states in each of motional modes in our simulation. After the repumping sequence, the ion is in  $|\downarrow\rangle$  and we apply additional heating to account for the electric field noise heating, which depends on heating rates and the total time spent on both the RSB pulse and the repumping process. Rabi rates are updated after a RSB pulse based on the Fock state distribution of secular modes to account for the Deybe-Waller effect.

In Fig. 7 (a), we plot the evolution of the mean Fock state occupation in all six motional modes during the sideband cooling process against the number of cooling pulses applied. For the two axial modes, the different cooling rate occurring around 100 pulses in the figure corresponds to the change from the 2<sup>nd</sup> order sideband cooling to the 1<sup>st</sup> order sideband cooling. As an example, we show the simulated Fock state distribution of the z-COM mode after sideband cooling in Fig. 7 (b). Besides the thermal-like distribution for the Fock states  $n < 3$ , our simulation shows a plateau probability distribution for Fock states  $n \gtrsim 5$ . Although the sum of the probability in the plateau distribution is too small to be observed in the experiment, our simulation indicates it usually contributes more than 50% of the total kinetic energy. In the z-COM mode, about 70% of the total energy is in the plateau distribution in the higher Fock states.

To include the energy contribution from this “hidden” population, we fit the simulated Fock state distribution to the linear combination of two thermal distributions to extract the mean occupation number  $\bar{n}_h$  characterizing the energy of the plateau distribution. Given  $\bar{n}_h$  as a fixed parameter, we then fit the RSB Rabi oscillation data shown in Fig. 3 in the main text to the double thermal distribution. Therefore the probability in the specific Fock state  $P(n)$  is expressed as

$$P(n) = \alpha P_{th}(n|\bar{n}_l) + (1 - \alpha) P_{th}(n|\bar{n}_h), \quad (6)$$

where  $\bar{n}_h$  is from the simulation and  $\bar{n}_l$  characterizes the energy in the lower Fock states. The probability  $P_{th}(n|\bar{n})$  represents the population probability in the Fock state  $|n\rangle$  of the thermal distribution with the average occupation  $\bar{n}$  and  $\alpha$  denotes the weight between two thermal distributions.

The double thermal fit result is plotted in Fig. 7 (b) compared with the simulated population. The least-squared fitting using the double thermal distribution model gives a factor of two to three smaller in  $\chi^2$  compared to the single thermal distribution model. The 95% confidence interval of the fit is used as the estimate of the energy upper bound and the results are shown in Fig. 3 in the main text. A bootstrapping method by resampling residuals is also performed to verify the energy

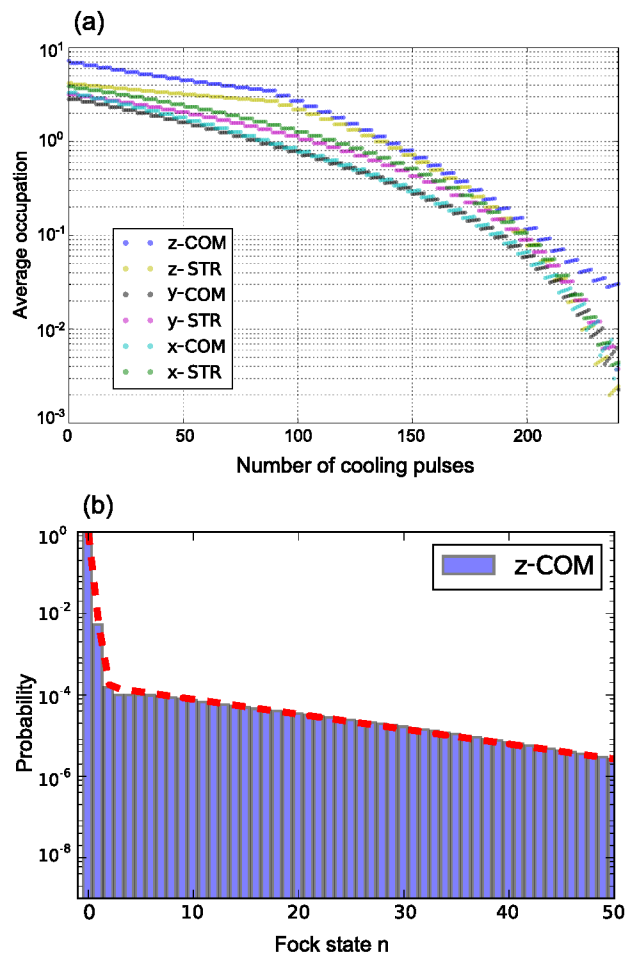


FIG. 7: (a) Evolution of the mean occupation of the six motional modes from the simulation versus the number of cooling pulses applied. (b) The simulated Fock state distribution in z-COM mode after sideband cooling. The red line represents the fitting to a double-thermal distribution with the mean occupation number to be 0.004 and 11, and the weight to be 0.99 and 0.01.

upper bound and the results are consistent with that from the least-squared fit [31]. The parameters of all secular modes and the estimates of the occupation number after sideband cooling are summarized in Table I. The heating rates due to different mechanisms discussed in the paper are shown in Table II.

### Heating Rate Measurement

To measure the heating rate of the motion due to the ambient electric field noise, we first sideband-cool the  $^{25}\text{Mg}^+ - ^{27}\text{Al}^+$  two-ion pair close to the motional ground state. Depending on the value of the heating rate, ions will then experience 10 to 30 ms of “dark time” without any cooling, such that the ions’ motion can heat due to

the ambient electric field noise. After the dark time, we measure the ratio of the RSB and the BSB transition probability to estimate the final occupation number of the ion in a specific motional mode and hence the heating rate. This sideband ratio method works well for determining heating rates but not for characterizing ions' energy after sideband cooling because the heating rapidly drives the Fock state distribution towards the thermal distribution [32, 33]. As a check of the constancy of the heating rate, repeated measurements of the heating rate in a specific secular mode were made for about an hour. These measurements were then repeated several times over several weeks to verify the long-term stability of the heating. The average and the standard error of heating rates are used to estimate the secular motion time-dilation shift. The measurements for one of six motional modes is shown in Fig. 8 and the values for all six modes are summarized in Table II.

### Shift and Uncertainty Estimate

For ions confined in a linear Paul trap, we must account for the intrinsic micromotion in the transverse secular modes of motion [34]. The contribution of the intrinsic (but not the excess) micromotion energy has been included when calculating the time-dilation shift in this paper. To determine the upper bound on the fractional time-dilation shift for a specific mode  $p$  at a given clock interrogation pulse duration  $t_i$ , we use  $\dot{\bar{n}}_p + 2\sigma$  values from Table II times  $t_i$  added with the upper bound of  $\bar{n}_{p,0}$  from Table I. For the lower bound we use  $\dot{\bar{n}}_p - 2\sigma$  values from Table II times  $t_i$  added with the lower range of  $\bar{n}_{p,0}$  from Table I. The bounds of the time-dilation shift of a specific mode  $p$  is given as

$$\begin{aligned} \left(\frac{\delta f}{f}\right)_p^{upper(lower)} &= \left(\frac{\delta\nu_p}{f}\right) \langle n_p(t_i)^{upper(lower)} \rangle \\ &= \left(\frac{\delta\nu_p}{f}\right) \left( \bar{n}_{p,0}^{upper(lower)} + \frac{1}{2}(\dot{\bar{n}}_p \pm 2\sigma)t_i \right), \end{aligned} \quad (7)$$

where  $\delta\nu_p$  denotes the secular motion time-dilation shift per quantum and  $\langle n_p(t_i) \rangle$  is the calculated average occupation number of the ion secular motion using Eq. (3) in the main text. Finally, we conservatively assume the shifts in six different secular modes are correlated, which should be the worst case, and use the average of the upper bound and lower bound as the estimate for the time-

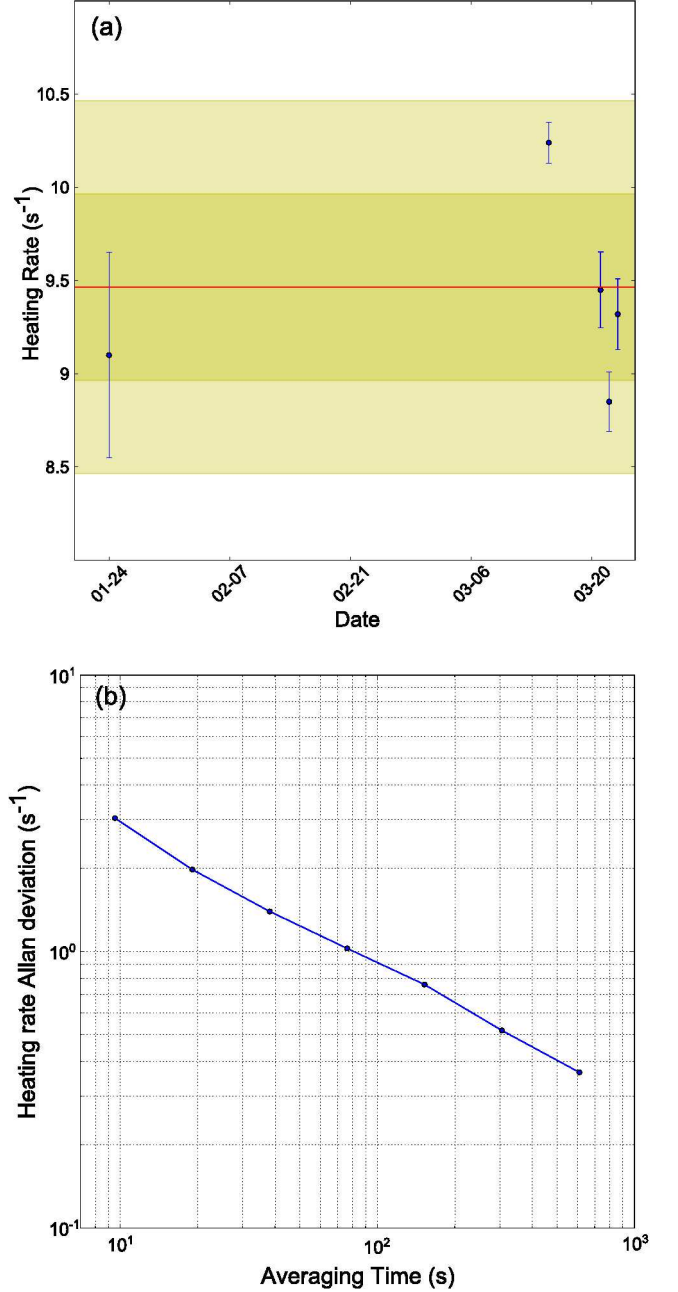


FIG. 8: The heating rate of the y-COM mode of motion for a  $^{25}\text{Mg}^+ - ^{27}\text{Al}^+$  two-ion pair. (a) Measurement of heating rate consisted of five experiments spanning several weeks. Error bars represent the statistical error. The red line and the yellow region are the mean value,  $1\sigma$  uncertainty, and  $2\sigma$  uncertainty. (b) Allan deviation of heating rate calculated from continuous measurement for about an hour.

dilation shift,

$$\left(\frac{\delta f}{f}\right)_{\text{secular}}^{\text{upper(lower)}} = \sum_p \left(\frac{\delta f}{f}\right)_p^{\text{upper(lower)}}, \quad (8)$$

$$\left(\frac{\delta f}{f}\right)_{\text{secular}} = \frac{\left(\frac{\delta f}{f}\right)_{\text{secular}}^{\text{upper}} + \left(\frac{\delta f}{f}\right)_{\text{secular}}^{\text{lower}}}{2}, \quad (9)$$

$$\text{uncertainty} = \frac{\left(\frac{\delta f}{f}\right)_{\text{secular}}^{\text{upper}} - \left(\frac{\delta f}{f}\right)_{\text{secular}}^{\text{lower}}}{2}. \quad (10)$$

The time dilation shift uncertainty due to secular motion in terms of the clock interrogation time represents by the blue region in Fig. 4(b) in the main text.

---

\* Electronic address: david.leibrandt@nist.gov

- [1] R. Blatt and D. J. Wineland, *Nature* **453**, 1008 (2008).
- [2] T. Rosenband, D. B. Hume, P. O. Schmidt, C. W. Chou, A. Brusch, L. Lorini, W. H. Oskay, R. E. Drullinger, T. M. Fortier, J. E. Stalnaker, S. A. Diddams, W. C. Swann, N. R. Newbury, W. M. Itano, D. J. Wineland, and J. C. Bergquist, *Science* **319**, 1808 (2008).
- [3] B. Lanyon, C. Hempel, D. Nigg, M. Müller, R. Gerritsma, F. Zähringer, P. Schindler, J. T. Barreiro, M. Rambach, G. Kirchmair, M. Hennrich, P. Zoller, R. Blatt, and C. F. Roos, *Science* **334**, 57 (2011).
- [4] C. Monroe and J. Kim, *Science* **339**, 1164 (2013).
- [5] T. Esslinger, T. Schaetz, and C. Monroe, *New. J. Phys.* **15**, 085009 (2013).
- [6] T. Monz, D. Nigg, E. A. Martinez, M. F. Brandl, P. Schindler, R. Rines, S. X. Wang, I. L. Chuang, and R. Blatt, *Science* **351**, 1068 (2016).
- [7] A. D. Ludlow, M. M. Boyd, J. Ye, E. Peik, and P. O. Schmidt, *Rev. Mod. Phys.* **87**, 637 (2015).
- [8] C. W. Chou, D. B. Hume, J. C. J. Koelemeij, D. J. Wineland, and T. Rosenband, *Phys. Rev. Lett.* **104**, 070802 (2010).
- [9] G. P. Barwood, G. Huang, H. A. Klein, L. A. M. Johnson, S. A. King, H. S. Margolis, K. Szymaniec, and P. Gill, *Phys. Rev. A* **89**, 050501 (2014).
- [10] N. Huntemann, C. Sanner, B. Lipphardt, C. Tamm, and E. Peik, *Phys. Rev. Lett.* **116**, 063001 (2016).
- [11] F. Diedrich, J. C. Bergquist, W. M. Itano, and D. J. Wineland, *Phys. Rev. Lett.* **62**, 403 (1989).
- [12] C. Monroe, D. M. Meekhof, B. E. King, S. R. Jefferts, W. M. Itano, D. J. Wineland, and P. Gould, *Phys. Rev. Lett.* **75**, 4011 (1995).
- [13] C. F. Roos, D. Leibfried, A. Mundt, F. Schmidt-Kaler, J. Eschner, and R. Blatt, *Phys. Rev. Lett.* **85**, 5547 (2000).
- [14] Y. Lin, J. P. Gaebler, T. R. Tan, R. Bowler, J. D. Jost, D. Leibfried, and D. J. Wineland, *Phys. Rev. Lett.* **110**, 153002 (2013).
- [15] S. Ejtemaee and P. C. Haljan, (2016), arXiv:1603.01248 [physics.atom-ph].
- [16] P. B. R. Nisbet-Jones, S. A. King, J. M. Jones, R. M. Godun, C. F. A. Baynham, K. Bongs, D. M., P. Balling, and P. Gill, *Appl. Phys. B* **122**, 57 (2016).
- [17] G. Poulsen, Y. Miroshnychenko, and M. Drewsen, *Phys. Rev. A* **86**, 051402(R) (2012).
- [18] Y. Wan, F. Gebert, F. Wolf, and P. O. Schmidt, *Phys. Rev. A* **91**, 043425 (2015).
- [19] Supplemental material.
- [20] Y. Colombe, D. H. Slichter, A. C. Wilson, D. Leibfried, and D. J. Wineland, *Opt. Express* **22**, 19783 (2014).
- [21] M. D. Barrett, B. DeMarco, T. Schaetz, V. Meyer, D. Leibfried, J. Britton, J. Chiaverini, W. M. Itano, B. Jelenković, J. D. Jost, C. Langer, T. Rosenband, and D. J. Wineland, *Phys. Rev. A* **68**, 042302 (2003).
- [22] D. J. Wineland, C. Monroe, W. M. Itano, D. Leibfried, B. E. King, and D. M. Meekhof, *J. Res. Natl. Inst. Stand. Technol.* **103**, 259 (1998).
- [23] Q. A. Turchette, C. J. Myatt, B. E. King, C. A. Sackett, D. Kielpinski, W. M. Itano, C. Monroe, and D. J. Wineland, *Phys. Rev. A* **62**, 053807 (2000).
- [24] W. M. Itano and D. J. Wineland, *Phys. Rev. A* **25**, 35 (1982).
- [25] R. Ozeri, W. M. Itano, R. B. Blakestad, J. Britton, J. Chiaverini, J. D. Jost, C. Langer, D. Leibfried, R. Reichle, S. Seidelin, J. H. Wesenberg, and D. J. Wineland, *Phys. Rev. A* **75**, 042329 (2007).
- [26] C. W. Chou, D. B. Hume, M. J. Thorpe, D. J. Wineland, and T. Rosenband, *Phys. Rev. Lett.* **106**, 160801 (2011).
- [27] T. Kessler, C. Hagemann, C. Grebing, T. Legero, U. Sterr, F. Riehle, M. J. Martin, L. Chen, and J. Ye, *Nature Photon.* **6**, 687 (2012).
- [28] S. Häfner, S. Falke, C. Grebing, S. Vogt, T. Legero, and M. Merimaa, *Opt. Lett.* **40**, 2112 (2015).
- [29] D. B. Hume and D. R. Leibbrandt, *Phys. Rev. A* **93**, 032138 (2016).
- [30] J. P. Gaebler, T. R. Tan, Y. Lin, Y. Wan, R. Bowler, A. C. Keith, S. Glancy, K. Coakley, E. Knill, D. Leibfried, and D. J. Wineland, *Phys. Rev. Lett* **117**, 060505 (2016).
- [31] T. J. DiCiccio and B. Efron, *Statist. Science* **3**, 189 (1996).
- [32] D. F. James, *Phys. Rev. Lett.* **81**, 317 (1998).
- [33] V. V. Dodonov, S. S. Mizrahi, and A. L. de Souza Silva, *J. Opt. B: Quantum Semiclass. Opt.* **2**, 271 (2000).
- [34] D. J. Wineland, W. Itano, J. Bergquist, and R. Hulet, *Phys. Rev. A* **36**, 2220 (1987).

TABLE I: Parameters of secular motion in a  $^{25}\text{Mg}^+ - ^{27}\text{Al}^+$  two-ion pair in the experiment.

	x-COM	x-STR	y-COM	y-STR	z-COM	z-STR
Frequency (MHz)	6.2	5.4	7.2	6.5	2.7	4.8
Lamb-Dicke parameter ( $^{25}\text{Mg}^+$ ) <sup>a</sup>	0.12	0.06	0.11	0.05	0.18	0.16
Time-dilation shift per quantum ( $10^{-18}$ ) <sup>b</sup>	-0.21	-0.85	-0.18	-0.86	-0.12	-0.18
Occupation number after sideband cooling (quantum) <sup>c</sup>	0-0.06	0-0.05	0-0.04	0-0.06	0-0.12	0-0.04

<sup>a</sup>calculated values for Raman cooling beams and consistent with experimental values.

<sup>b</sup>including the shift due to the intrinsic micromotion in the transverse directions.

<sup>c</sup>95% confidence interval.

TABLE II: Summary of heating rates due to different mechanisms considered in the simulation.

	x-COM	x-STR	y-COM	y-STR	z-COM	z-STR
Repumping sequence (quantum/cycle) <sup>a</sup>	0.015	0.004	0.012	0.002	0.027	0.017
Raman scattering ( $\mu\text{s}^{-1}$ ) <sup>b</sup>	$< 10^{-4}$	$< 10^{-4}$	$< 10^{-4}$	$< 10^{-4}$	$< 10^{-4}$	$< 10^{-4}$
Rayleigh scattering ( $\mu\text{s}^{-1}$ ) <sup>b</sup>	$< 10^{-4}$	$< 10^{-4}$	$< 10^{-4}$	$< 10^{-4}$	$< 10^{-4}$	$< 10^{-4}$
Off-resonant coupling (quantum/pulse) <sup>c</sup>	$3.9 \times 10^{-4}$	$3.6 \times 10^{-4}$	$2.1 \times 10^{-4}$	$3.3 \times 10^{-4}$	$1.6 \times 10^{-3}$	$6.5 \times 10^{-4}$
Spontaneous decay + RSB (quantum/pulse) <sup>b,c</sup>	$1.4 \times 10^{-3}$	$2.6 \times 10^{-3}$	$1.5 \times 10^{-3}$	$3.1 \times 10^{-3}$	$7.5 \times 10^{-4}$	$9.1 \times 10^{-4}$
Electric field noise ( $\text{s}^{-1}$ ) <sup>a,d</sup>	$11.95 \pm 0.64$	$1.94 \pm 0.08$	$9.47 \pm 1.00$	$1.96 \pm 0.18$	$9.12 \pm 0.32$	$0.34 \pm 0.02$

<sup>a</sup>experimental measurement.

<sup>b</sup>estimate using the measured depumping rate from  $|\downarrow\rangle$  to  $|\uparrow\rangle$  by blue Raman beams.

<sup>c</sup>motional excitation from ground state, simulation.

<sup>d</sup> $2\sigma$  uncertainty